APL Photonics

High-efficiency lithium niobate modulator for K band operation

Cite as: APL Photonics 5, 091302 (2020); https://doi.org/10.1063/5.0020040
Submitted: 27 June 2020 • Accepted: 06 September 2020 • Published Online: 18 September 2020

Abu Naim R. Ahmed, Shouyuan Shi, Andrew Mercante, et al.

AIP Publishing

High-efficiency lithium niobate modulator for K band operation

Cite as: APL Photon. 5, 091302 (2020); doi: 10.1063/5.0020040
Submitted: 27 June 2020 • Accepted: 6 September 2020 •
Published Online: 18 September 2020

Abu Naim R. Ahmed,[1,a)] Shouyuan Shi,[1] Andrew Mercante,[2] Sean Nelan,[1] Peng Yao,[2] and Dennis W. Prather[1,2]

AFFILIATIONS

[1]School of Electrical and Computer Engineering, University of Delaware, Newark, Delaware 19716, USA
[2]Phase Sensitive Innovations, Newark, Delaware 19711, USA

[a)]**Author to whom correspondence should be addressed:** naimece@udel.edu

ABSTRACT

This paper reports a hybrid silicon nitride–lithium niobate electro-optic Mach–Zehnder-interferometer modulator that demonstrates overall improvements in terms of half-wave voltage, optical insertion loss, extinction ratio, and operational bandwidth. The fabricated device exhibits a DC half-wave voltage of ~1.3 V, a static extinction ratio of ~27 dB, an on-chip optical loss of ~1.53 dB, and a 3 dB electro-optic bandwidth of 29 GHz. In addition, this device operates beyond the 3 dB bandwidth, where a half-wave voltage of 3 V is extracted at 40 GHz when the device is biased at quadrature. The modulator is realized by strip-loading thin-film lithium niobate with low-pressure chemical vapor deposited silicon nitride; this enables reduced on-chip losses and allows for a lengthened 2.4 cm long interaction region that is specifically engineered for broadband performance.

I. INTRODUCTION

The electro-optic (EO) modulator is a vital component in the context of photonic integrated circuits (PICs) and a technological pillar of modern information technology. The bulk modulator has widespread use in fiber optic communication networks, where the demand for higher bandwidths and data rates are becoming increasingly necessary. However, the bulk EO modulator is not ideal for PICs as these modulators need to address critical figures of merit (FOM), such as size, weight, power consumption, cost, and performance (SWaP-CP). With this, the ideal FOM for an EO modulator are low voltage operation, ultra-high bandwidth, high linearity, a high extinction ratio, and low optical and RF absorption loss.

Currently, most PICs are made from silicon (Si) and III–V materials, which are widely available and are supported by the well-developed manufacturing processes. However, these materials are inherently problematic for high-power and ultra-high-frequency operation due to their high third-order nonlinear coefficients $(\chi)^3$, higher propagation loss,[1–3] and a relatively low Pockels coefficient[4] compared to other oxide-based ferroelectric materials (e.g., $LiNbO_3$). For example, the $(\chi)^3$ of Si, GaAs, and InP are 2×10^{-10} esu, 1×10^{-10} esu, and 7.86×10^{-10} esu, respectively. All of these are three orders of magnitude larger than what is exhibited by lithium niobate ($LiNbO_3$), which is nearly 7.45×10^{-13} esu.[5] Moreover, III–V materials must be epitaxially grown from the underlying layer.

As a result, the bulk $LiNbO_3$ based modulator, as a discrete device, has received widespread use in optical communication over the last few decades. It offers very large operational bandwidths, system linearity, and negligible chirping. The half-wave voltage (V_π) for a commercial off-the-shelf (COTS) bulk $LiNbO_3$ Mach–Zehnder modulator (MZM) is 3 V–4 V, with a 3 dB bandwidth of 40 GHz for a 4 cm–5 cm device length.[6] However, the index contrast between the core and cladding is ~0.02, which corresponds to a minimum bending radius of more than a few centimeters.[7] The optical mode size is roughly 100 μm^2; thus, the modulated electrodes are spaced further apart to avoid metal absorption loss. Consequently, there is poor electrical and optical mode overlap, which results in a large V_π. Thus, a $LiNbO_3$-based PIC chip is not realizable using a bulk device, as the key building block of PICs requires sharp, sub-millimeter waveguide bends and low drive voltage.

Recently, a crystal ion-sliced (CIS) thin-film of lithium niobate on insulator (TFLNOI) has been shown to reduce the optical mode size, which results in more RF-mode overlap and smaller bending radii.[8,9] In such a layer, the optical field diameter shrinks to just ~2% of its size in bulk material and the electrodes can be brought much closer to the waveguide, which improves field strength and lowers the V_π. With its low voltage operation, high index contrast (~0.7), and commercial availability, the TFLNOI modulator is an ideal choice for PIC. Furthermore, thin-film technology helps to easily match the RF effective phase index and optical group index, an important design parameter in realizing broadband modulator operation.[10] However, $LiNbO_3$ suffers from difficult micro-structuring in comparison to silicon-based materials due to its chemically inert and low toughness properties.[11] Thus, a more conventional film is loaded on the TFLNOI to enable waveguiding in the $LiNbO_3$ without etching the $LiNbO_3$ itself. To date, different material systems have been investigated for use as the loading material on $LiNbO_3$, such as Si–$LiNbO_3$,[12,13] silicon carbide (SiC)–$LiNbO_3$,[14] chalcogenide glass (ChG)–$LiNbO_3$,[15] tantalum pentoxide (Ta_2O_5)–$LiNbO_3$,[16] and silicon nitride (Si_3N_4)–$LiNbO_3$.[17] Various photonic structures, including MZM,[12,13,16,18] micro-ring modulators,[19] and mode transition structures,[12,13] have been demonstrated in these platforms. A motivation to work with the Si_3N_4 platform includes ultra-low propagation loss, high optical power carrying capacity, and CMOS compatibility.[17,20] The addition of Si_3N_4 to the $LiNbO_3$ device layer increases the overall theoretical minimum for propagation loss in an optical device. At a wavelength of 1550 nm, the material absorption limit for $LiNbO_3$ is reported below 0.002 dB/cm,[21] and low-pressure chemical vapor deposition (LPCVD) Si_3N_4 demonstrates propagation loss of the same magnitude reported at 0.005 dB/cm.[22]

To achieve an effective PIC and RF link, low voltage modulator operation is of utmost importance. Presently, ultra-low-voltage CMOS technology has brought supply voltages from 5 V down top 1.5 V, while some chips require only 0.8 V.[23] These lower drive voltages facilitate lower energy consumption and allow the EO modulator to be used on-chip without an external digital to analog converter (DAC) or a low-noise amplifier (LNA). The low-voltage operation of the $LiNbO_3$ modulator is highly desirable for an RF link to maintain a low noise figure, high gain, and acceptable spurious-free dynamic range.[24] In an attempt to fulfill these requirements, we have developed a 2.4 cm hybrid Si_3N_4–$LiNbO_3$ MZM with a V_π of 1.3 V and a 3 dB bandwidth of 29 GHz. This is an incremental improvement to the current state-of-the-art in this same hybrid platform, a 1.2 cm long device possessing a V_π of 2.5 V and a 3 dB bandwidth of 8 GHz.[18] The previously cited state-of-the-art hybrid Si_3N_4–$LiNbO_3$ MZM also exhibits a high on-chip loss of 5.4 dB due to the use of plasma-enhanced chemical vapor deposition (PECVD) Si_3N_4 rather than LPCVD.[17]

II. DEVICE DESIGN

The 3D schematic structure of the MZM in the hybrid Si_3N_4–$LiNbO_3$ platform is shown in Fig. 1(a). The modulator's electrodes are implemented using a push–pull MZM configuration. The optical signal is equally split into two paths, and each arm is modulated by opposite electric fields directed by an applied voltage to the co-planar ground-signal-ground (GSG) electrodes. A multimode interferometric (MMI) splitter and combiner are used as a 3-dB coupler for the MZM configuration. The dimension of the 3 dB MMI coupler is 38 × 7.2 μm^2; the single-mode optical waveguide leading up to the multimode region is tapered from 1.5 μm to 3 μm over a length of 80 μm. This taper is intended to reduce optical loss due to mode mismatch related reflections.[17] The cross section of the modulator interaction region is shown in Fig. 1(b); the substrate consists of an ~200 nm thick LPCVD Si_3N_4 strip on top of 300 nm of *X*-cut thin-film $LiNbO_3$ (H_{LN}), with a 4.7 μm SiO_2 bottom cladding layer. The stack of thin films is affixed to a high resistivity Si wafer. The main reason for choosing *X*-cut TFLNOI over *Z*-cut TFLNOI is threefold: (i) easy fabrication process and packaging by directly patterning the electrodes on top of the TFLNOI layer, (ii) low drive voltage and low optical absorption loss as no buffer layer is required, and (iii) more symmetric design in the intensity modulator with a push–pull configuration, leading to high extinction and chirp-free modulation. The width (W_{SiN}) and thickness (T_{SiN}) of the strip loaded waveguide are 1.5 μm and 200 nm, respectively, which laterally confines the fundamental transverse electric (TE) mode in the $LiNbO_3$. TE mode is desired for the *X*-cut $LiNbO_3$ modulator to efficiently utilize the maximum Pockels coefficient of $LiNbO_3$, i.e., r_{33} ~ 31 pm/V. The optical mode profile at one of the modulator arms is depicted in Fig. 1(c), where the mode confinement factor in the $LiNbO_3$ is ~65% for this configuration when simulated in the Lumerical MODE Solver. The simulated optical group index (n_{Og}) of the optical mode is found to be 2.18 for the fundamental TE mode. The optical mode area of the hybrid waveguide is roughly 1.0 μm^2. The well-concentrated optical mode allows for the electrodes to be closer together without incurring additional metal absorption loss.

The operational bandwidth of the EO modulator is determined by an RF impedance mismatch, index mismatch, and RF losses. These parameters need to be accounted for during the design of the traveling wave co-planar waveguide (CPW). Typically, the source and termination impedance of RF cables and probes is equivalent to 50 Ω. As such, the characteristic impedance (Z_{CPW}) of the CPW is engineered to be 50 Ω to minimize reflections from the source. The mismatch between the n_{Og} and RF effective phase index (n_{RF}) is defined as the index mismatch. Bulk $LiNbO_3$ has a much higher effective RF index (~6) than the optical group index (~2.2).[25] Thus, many previously demonstrated index matching techniques require additional fabrication processes (e.g., substrate thinning, thicker electrodes by electroplating, and buffer oxide layer). The thin-film $LiNbO_3$ has an inherently low RF effective index compared to bulk due to the presence of only a thin device layer of the high index $LiNbO_3$ being surrounding by low RF index materials such as Si and SiO_2. The reduced RF index of the substrate allows for more straightforward index matching when compared to bulk $LiNbO_3$. The design parameters of the CPW electrodes are thickness (T_{Au}) and width (W_s) of the signal electrode, as well as the electrode gap (W_{gap}) between the signal and ground. The RF losses in our CPW that are expected to limit device performance are conduction loss (α_m) and dielectric loss (α_d). A CPW with a wider and taller signal electrode can help to reduce conduction loss in the transmission line. However, an unoptimized thick electrode can introduce an additional index mismatch. The total RF insertion loss and velocity mismatch increase with the modulator length, thus limiting the modulator bandwidth. Although a longer electrode length reduces the half-wave voltage, the bandwidth of the modulator also decreases

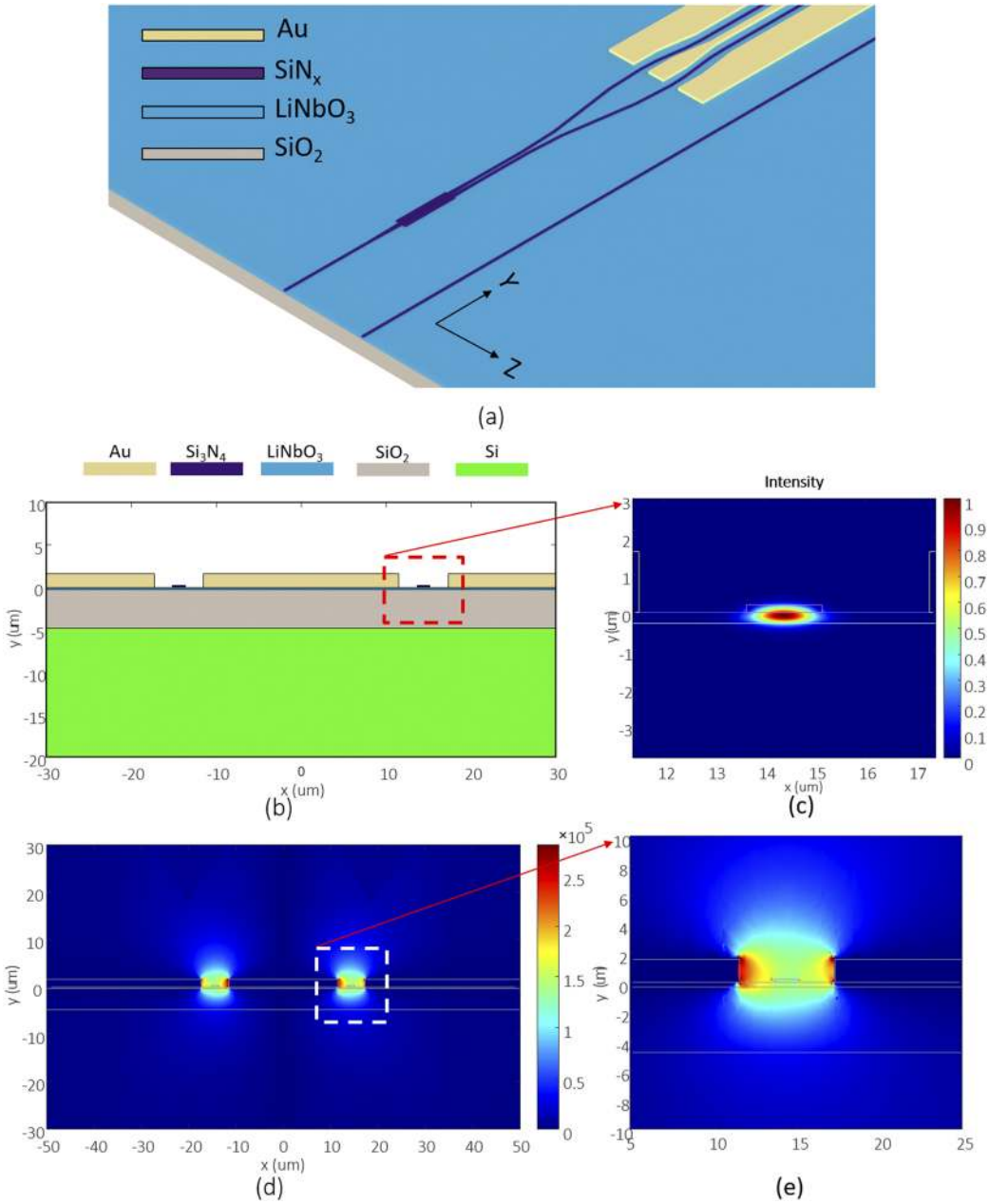

FIG. 1. (a) 3D schematic of the MZM, (b) cross-sectional view of the MZM, (c) simulated optical TE mode profile of the waveguide, (d) simulated CPW mode distribution with 1 V driving voltage between the signal and ground electrodes, and (e) close view of the CPW mode profile in single MZM arms.

significantly.[26] As such, an optimal RF electrode design is required to obtain a fine balance between the minimal RF loss, better index matching, and 50 Ω characteristic impedance. The CPW transmission line is modeled by the finite element method (FEM) using HFSS, Ansys. The fabricated electrode dimensions in the modulator's interaction region are a thickness (T_{Au}) of ~1.8 μm, a signal width (W_s) of 23 μm, and a gap (W_{gap}) of 5.8 μm. A 500 μm long taper is used to transition from the launch region to the interaction region. At the RF probe launch region, the probe pad signal width and electrode gap are 70 μm and 14 μm, respectively. The simulated electric field distribution is shown in Figs. 1(c) and 1(d), a peak field of ~1.25×10^5 V/m is observed for a driving voltage of 1 V between the signal and ground electrodes. The simulated Z_{CPW} is ~43 Ω up to 60 GHz, as shown in Fig. 2(a). The simulated RF loss for this CPW

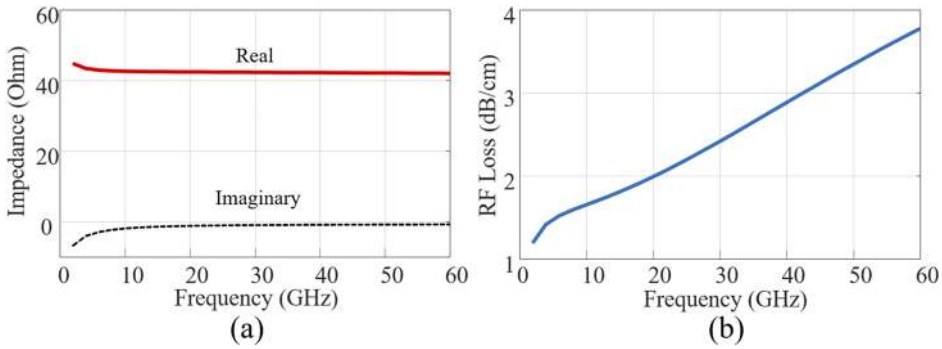

FIG. 2. CPW characterization of a 2.4 cm hybrid MZM: (a) the simulated impedance of the CPW over the frequency range up to 60 GHz and (b) simulated RF loss of the designed CPW.

is plotted in Fig. 2(b). The simulated n_{RF} converges to ~2.05 above 15 GHz. The index matching method is discussed in Sec. III. Once both RF and optical fields are available, by calculating the mode overlap between the simulated RF and optical modes, the DC V_π of the proposed modulator is found to be 1.18 V for the device with a length of 2.4 cm. The corresponding $V_\pi L$ is 2.83 V.cm.

III. DEVICE FABRICATION

The hybrid device fabrication starts with a 200 nm Si_3N_4 deposition on the 300 nm *X*-cut TFLNOI, which is procured from NanoLN^{TM}. The bottom cladding of the $LiNbO_3$ includes 4.7 μm of SiO_2 on the top of high resistivity (~10 kΩ cm) Si wafers. The Si handle provides a higher thermal budget than the quartz handle, which is essential for the high-temperature LPCVD deposition process. Electron-beam lithography (EBL) and dry etching are used to define optical waveguides and MZM in Si_3N_4 using a similar process as described in our previous work.[17] The co-planar waveguide (CPW) electrodes are directly patterned on top of the $LiNbO_3$ using a gold electroplating process. The CPW electrode fabrication process consists of the following steps: (i) seed layer deposition, (ii) laser lithography, (iii) electroplating, and (iv) seed layer and photoresist stripping. A ~1.8 μm thick Au is electroplated using 0.8 mA current for 1 h. The final step is dicing and polishing the waveguide's end-facets to prepare a clean waveguide facet for efficient fiber-chip coupling and minimal scattering loss. The sample's end-facets are gradually polished at a 15° angle to its optical axis using diamond lapping film discs from Allied High-Tech Products, Inc. after the

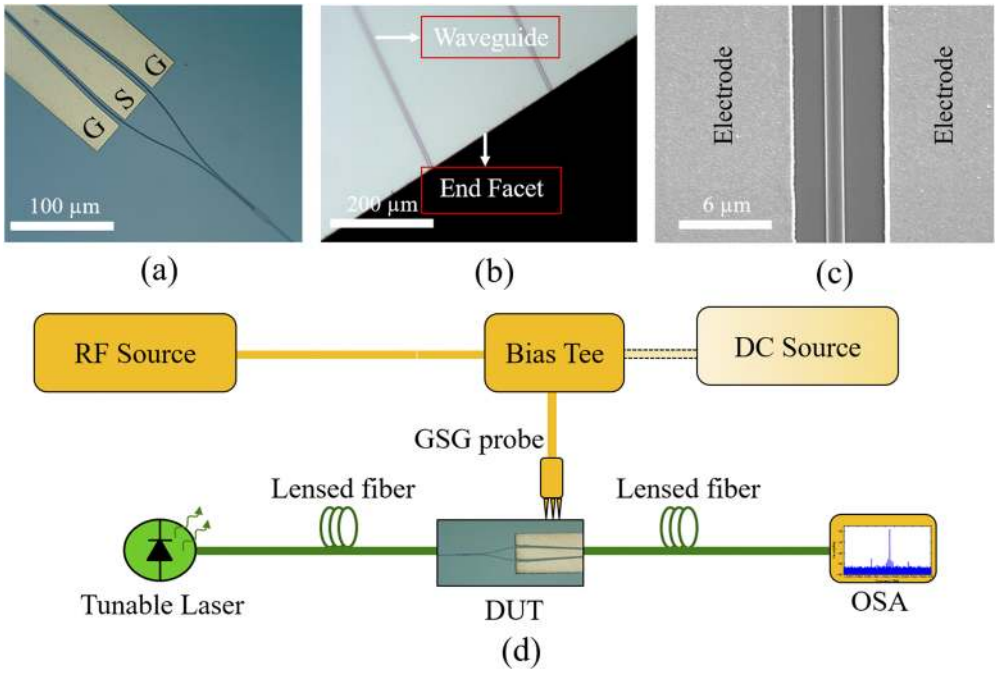

FIG. 3. (a) Microscope image of the fabricated MZM with the integrated CPW electrode, (b) microscope image of the waveguide end-facets after dicing and polishing steps, (c) SEM image of the MZM interaction region, and (d) schematic of the experimental setup for measuring the sideband power of the MZM.

dicing step. Scanning electron microscope (SEM) images and microscope images of various parts of the fabricated hybrid devices are shown in Figs. 3(a)–3(c). These include an optical modulator with an integrated electrode, polished end facet of the waveguide, and modulator interaction section.

IV. MACH–ZEHNDER MODULATOR CHARACTERIZATION

A. Optical characterization

For the waveguide characterization, the output of the tunable laser (Keysight 81608A) is set at an operating wavelength of 1550 nm, which is coupled to the fabricated waveguide end-facet via a ~2.5 μm Mode Field Diameter (MFD) polarized maintaining lensed fiber (OZ optics). The light exiting the waveguide is coupled to the output lensed fiber, which is connected to an optical power meter to measure the output power. The propagation loss of the LPCVD Si_3N_4 based hybrid waveguides is ~0.28 dB/cm, measured by the cutback method. At peak transmission near 1550 nm, the total optical insertion loss of the 2.4 cm long MZM is ~13.86 dB. The calculated on-chip loss is about ~1.53 dB, which included propagation loss, metal-induced absorption loss, and MMI loss. The simulated (Lumerical software package) metal-induced absorption loss for the 6 μm electrode gap is ~0.02 dB/cm, so the additional ~0.1 dB loss is likely due to MMI loss. The majority of the insertion loss is a result of the coupling loss due to the mode mismatch between the lensed fiber and the optical waveguide.

B. Electro-optic characterization

The MZM functionality, as an EO transducer, is characterized at low frequencies by directly measuring V_π at heightened frequencies; the observed intensity of the modulated optical sidebands is our chosen metric. In addition to the sideband power, we measure the RF scattering parameters (S-parameters) of the CPW to characterize the electrodes. A low-speed (150 kHz) triangular voltage wave is applied to the modulator electrode via DC needle probes. For the push–pull configuration, the center arm is probed with a positive voltage and the other two arms are grounded. Thus, the first arm's phase change is complementary to that of the second arm. To measure V_π, the MZM optical output is directed into a photodetector, and the current produced by the photodetector is converted to a voltage with a trans-impedance amplifier this voltage is observed on an oscilloscope alongside the applied modulating signal. The applied voltage that causes the amplitude modulation trace to go from a minimum to its nearest maximum is called the DC V_π, as shown in Fig. 4(a). The measured DC V_π is 1.3 V for the 2.4 cm long MZM, which agrees with the simulated DC V_π. The corresponding voltage-length product is 3.12 V cm. The static extinction ratio is ~27 dB, which is obtained by plotting the normalized optical transmission in a logarithmic scale [Fig. 4(b)].

The high-frequency EO response of the MZM is characterized by measuring the sideband power while applying a modulating RF signal to the electrodes. The experimental setup for the sideband generation is shown in Fig. 3(d). The RF signal is generated by a signal generator (N5183 MXG for 0 GHz–40 GHz). A 50 Ω high-frequency GSG probe with a high operational bandwidth of 67 GHz is used for signal launch on the electrode pad. While measuring the sidebands, the modulator is biased at quadrature using a DC source. At quadrature, the modulator operates at its most linear region of the transmission curve. A bias tee is used to launch both RF and DC signals into the device under test through the GSG probe. The device's modulated output signal is fed into the APEX AP 2083A optical spectrum analyzer (OSA) where the intensity of the modulation sideband is observed. The modulation spectrum is normalized to the optical carrier input. The RF feed loss and probe insertion loss are accounted for as well during the sideband normalization. The normalized modulation spectra at the quadrature of the MZM are shown in Fig. 5(a). The extinction ratio of the MZM is ~25 dB, extracted from the null and peak bias modulation spectrum (supplementary material, Sec. I). The measured 3 dB bandwidth of this device is ~24 GHz (supplementary material, Sec. II). The sideband power roll-off from low frequency to 40 GHz is about 8 dB. The unmatched n_{RF} and n_{Og} cause this sporadic roll-off after the 3 dB point. To further confirm this index mismatch, we measured the S-parameter of the traveling-wave CPW. The measured S-parameters are shown in Fig. 5(b). The high reflection at the lower frequency (DC to 4 GHz) is causing the initial drop of the modulator's sideband power. This is also visible from the impedance as a function of the frequency curve extracted from the S-parameter[27,28] [Fig. 6(a)]. The impedance is almost constant after 5 GHz. A Z_{CPW} of ~45.44 Ω and an n_{RF} of 2.052 are obtained using the data fitting with the measured S-parameter.[27,28] The index mismatch for this device is ~0.13 [Fig. 6(b)], which is one of the main limiting factors of the

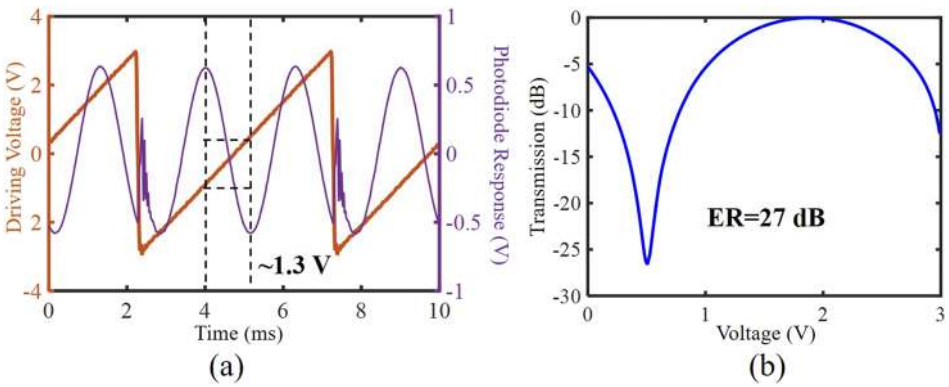

FIG. 4. (a) The amplitude modulation trace of the MZM in the hybrid platform and (b) the measured extinction ratio of the hybrid modulator in dB.

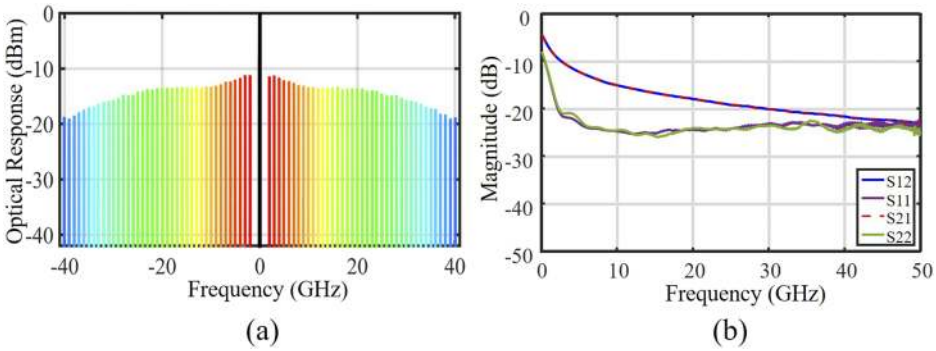

FIG. 5. MZM characterization with air-clad: (a) the normalized modulation spectra up to 40 GHz of the quadrature bias MZM for a 1550 nm optical carrier and (b) the measured S-parameters of the traveling-wave CPW with the air-clad interaction region.

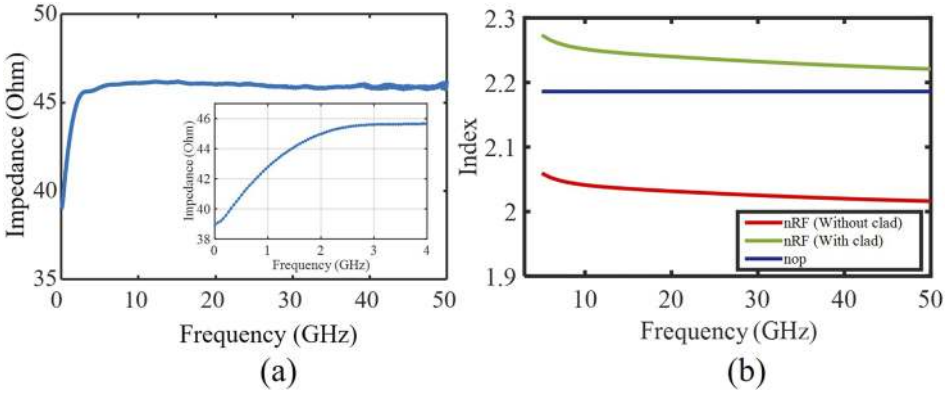

FIG. 6. (a) The Z_{CPW} extracted from the S-parameter plotted against the modulation frequency. The inset shows the magnified version of impedance from 0 GHz to 4 GHz. (b) Simulated indices are plotted. The red and green traces represent the simulated RF effective phase indices of a device under air cladding and UV-15 cladding, respectively. The simulated n_{Og} is shown in the blue trace.

broadband operation of the modulator. The traveling-wave electrode's conduction loss, as a function of frequency, also limits modulator performance (supplementary material, Sec. III). The 3 dB bandwidth of the modulator can be improved by cladding the modulator's interaction region with a higher index material than the air. The high index-cladding increases the n_{RF} and reduces the index mismatch. By adding an ultra-violet (UV) adhesive cladding layer, the simulated n_{RF} improves from 2.05 to 2.21 at 40 GHz [Fig. 6(b)]. A thick UV15 cladding layer is applied to the modulator's interaction region via soft brushing and then exposed to UV light for complete stabilization. The sideband power is measured for the UV15-clad MZM device up to 40 GHz, as shown in Fig. 7(a). The 3 dB bandwidth of this device is ~29 GHz, which is ~6 GHz broader than the air-clad device. Furthermore, the UV15 clad MZM shows a steady roll-off of ~4.5 dB up to 40 GHz, which promises high-frequency operation beyond 50 GHz. The measured S-parameter of the UV-15 clad CPW is shown in Fig. 7(b). The extracted n_{RF} from the S-parameters is 2.27 for the UV15-clad CPW. The simulated optical group index is 2.168. Thus, the UV15-clad device still experiences an index mismatch of ~0.1.

Nonetheless, our MZM still represents increased 3 dB bandwidth, reduced operation voltage, and lower insertion loss compared to previously demonstrated hybrid Mach–Zehnder-Interferometer (MZI) modulators in this platform.[18,29] The comparison between

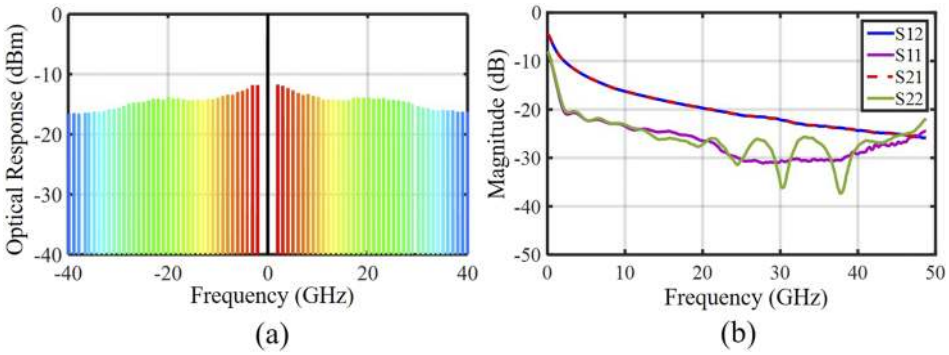

FIG. 7. MZM characterization with UV15-clad. (a) The normalized modulation spectra up to 40 GHz of the quadrature bias MZM for the 1550 nm optical carrier. The 3 dB bandwidth observed for the MZM is 29 GHz. (b) The measured S-parameters of the CPW.

TABLE I. Comparison between our hybrid TFLNOI MZM and other competing platforms.

Type	Length (cm)	V_π (V)	$V_\pi L$ (V cm)	Bandwidth (GHz)	On-chip loss (dB)	References
Si	0.2	4.1	0.74	34	7.6	30
InP	0.36	1.5	0.54	67	2.0	31
Bulk LN	>2	4.5–4.9	>10	40	N/A	6
Plasmonics	0.001	6	0.006	70	2.5	32
Polymer	0.05	22	1.1	100	2.5	33
Photonic crystal	0.03	0.93	0.028	15	~8	34
Si on TFLNOI	0.5	5.1	2.55	>70	<2.5	12
Standalone TFLNOI	2	1.4	2.8	45	0.4	8
Si_3N_4 on TFLNOI	1.2	2.5	3.0	8	>8.4	18
Si_3N_4 on TFLNOI	2.4	1.3	3.12	29	1.53	This work

our hybrid MZM and other competing state-of-the-art MZMs is shown in Table I. The designed CPW is not the most-optimized CPW, and further optimization of the RF design is possible by (i) matching the impedance between the launch electrodes and probe, (ii) improving index or velocity match, and (iii) reducing conduction loss via electroplating quality.

V. CONCLUSION

To conclude, we have demonstrated a low half-wave voltage, high 3 dB bandwidth, and low propagation loss MZM in a hybrid Si_3N_4–$LiNbO_3$ platform. To the best of our knowledge, this is the lowest half-wave voltage with a 3 dB bandwidth demonstrated beyond 20 GHz in this hybrid platform. The half-wave voltage and 3 dB bandwidth are comparable with the state-of-the-art MZM shown in the standalone TFLNOI platform.[8] Moreover, there is a clear path to further improve the modulator's performance by adjusting the CPW design for application-specific devices. The modulator's performance makes it a suitable candidate for emerging technologies including coherent transceivers for telecommunication,[35] data center optical interconnects,[36] and antenna remoting and phased array.[37]

SUPPLEMENTARY MATERIAL

See the supplementary material for additional data and methods that support the main conclusions in this paper.

ACKNOWLEDGMENTS

The authors acknowledge support from the Multidisciplinary University Research Initiative (MURI) program through the Air Force Office of Scientific Research (AFOSR), Dr. Gernot Pomrenke from the AFOSR and the National Science Foundation (Grant No. NSF ECCS-1509081). Main Funding Source: Air Force Office of Scientific Research (AFOSR) (Project No. FA9550-17-1-0071).

DATA AVAILABILITY

The data that support the findings of this study are available from the corresponding author upon reasonable request.

REFERENCES

[1] R. Baets, A. Z. Subramanian, S. Clemmen, B. Kuyken, P. Bienstman, N. Le Thomas, G. Roelkens, D. Van Thourhout, P. Helin, and S. Severi, in *Optical Fiber Communication Conference* (Optical Society of America, 2016), p. Th3J.1.
[2] M. Smit, K. Williams, and J. Van Der Tol, APL Photonics **4**, 050901 (2019).
[3] J. Wang, A. Santamato, P. Jiang, D. Bonneau, E. Engin, J. W. Silverstone, M. Lermer, J. Beetz, M. Kamp, S. Höfling, M. G. Tanner, C. M. Natarajan, R. H. Hadfield, S. N. Dorenbos, V. Zwiller, J. L. O'Brien, and M. G. Thompson, Opt. Commun. **327**, 49–55 (2014).
[4] A. Yariv and P. Yeh, *Photonics: Optical Electronics in Modern Communications*, The Oxford Series in Electrical and Computer Engineering (Oxford University Press, 2006).
[5] H. Li, F. Zhou, X. Zhang, and W. Ji, Appl. Phys. B **64**, 659 (1997).
[6] See http://www.eospace.com/low-v-compact-xcut-modulator for Eospace Advanced Products, 2020.
[7] R. G. Hunsperger, *Integrated Optics* (Springer, 1995).
[8] C. Wang, M. Zhang, X. Chen, M. Bertrand, A. Shams-Ansari, S. Chandrasekhar, P. Winzer, and M. Lončar, Nature **562**(7725), 101–104 (2018).
[9] A. Honardoost, K. Abdelsalam, and S. Fathpour, Laser Photonics Rev. **14**(9), 2000088 (2020).
[10] A. J. Mercante, S. Shi, P. Yao, L. Xie, R. M. Weikle, and D. W. Prather, Opt. Express **26**, 14810 (2018).
[11] D. Huo, Z. J. Choong, Y. Shi, J. Hedley, and Y. Zhao, J. Micromech. Microeng. **26**, 095005 (2016).
[12] M. He, M. Xu, Y. Ren, J. Jian, Z. Ruan, Y. Xu, S. Gao, S. Sun, X. Wen, L. Zhou, L. Liu, C. Guo, H. Chen, S. Yu, L. Liu, and X. Cai, Nat. Photonics **13**, 359 (2019).
[13] P. O. Weigel, J. Zhao, K. Fang, H. Al-Rubaye, D. Trotter, D. Hood, J. Mudrick, C. Dallo, A. T. Pomerene, and A. L. Starbuck, Opt. Express **26**(18), 23728–23739 (2018).
[14] P. O. Weigel and S. Mookherjea, J. Opt. Soc. Am. B **35**, 593 (2018).
[15] A. Rao, A. Patil, P. Rabiei, A. Honardoost, R. DeSalvo, A. Paolella, and S. Fathpour, Opt. Lett. **41**, 5700 (2016).
[16] P. Rabiei, J. Ma, S. Khan, J. Chiles, and S. Fathpour, Opt. Express **21**, 025573 (2013).
[17] A. N. R. Ahmed, S. Nelan, S. Shi, P. Yao, A. Mercante, and D. W. Prather, Opt. Lett. **45**, 1112 (2020).
[18] S. Jin, L. Xu, H. Zhang, and Y. Li, IEEE Photonics Technol. Lett. **28**, 736 (2015).
[19] A. N. R. Ahmed, S. Shi, M. Zablocki, P. Yao, and D. W. Prather, Opt. Lett. **44**, 618 (2019).
[20] J. F. Bauters, M. J. R. Heck, D. John, D. Dai, M.-C. Tien, J. S. Barton, A. Leinse, R. G. Heideman, D. J. Blumenthal, and J. E. Bowers, Opt. Express **19**, 3163 (2011).
[21] V. S. Ilchenko, A. A. Savchenkov, A. B. Matsko, and L. Maleki, Phys. Rev. Lett. **92**, 043903 (2004).
[22] T. A. Huffman, G. M. Brodnik, C. Pinho, S. Gundavarapu, D. Baney, and D. J. Blumenthal, IEEE J. Sel. Top. Quantum Electron. **24**, 1 (2018).

[23]D. A. B. Miller, J. Lightwave Technol. **35**, 346 (2017).
[24]D. Marpaung, J. Yao, and J. Capmany, Nat. Photonics **13**, 80 (2019).
[25]J. Macario, P. Yao, S. Shi, A. Zablocki, C. Harrity, R. D. Martin, C. A. Schuetz, and D. W. Prather, Opt. Express **20**, 23623 (2012).
[26]J. A. I. Fuste and M. C. S. Blanco, Opt. Lett. **38**, 1548 (2013).
[27]D. M. Pozar, *Microwave Engineering* (John Wiley & Sons, 2009).
[28]P. O. Weigel, "High-speed hybrid silicon-lithium niobate electro-optic modulators & related technologies," Ph.D. thesis, UC San Diego, 2018.
[29]N. Boynton, H. Cai, M. Gehl, S. Arterburn, C. Dallo, A. Pomerene, A. Starbuck, D. Hood, D. C. Trotter, T. Friedmann, C. T. DeRose, and A. Lentine, Opt. Express **28**, 1868 (2020).
[30]S. S. Azadeh, F. Merget, S. Romero-García, A. Moscoso-Mártir, N. von den Driesch, J. Müller, S. Mantl, D. Buca, and J. Witzens, Opt. Express **23**, 023526 (2015).
[31]Y. Ogiso, J. Ozaki, Y. Ueda, N. Kashio, N. Kikuchi, E. Yamada, H. Tanobe, S. Kanazawa, H. Yamazaki, and Y. Ohiso, J. Lightwave Technol. **35**, 1450 (2016).
[32]C. Haffner, W. Heni, Y. Fedoryshyn, J. Niegemann, A. Melikyan, D. L. Elder, B. Baeuerle, Y. Salamin, A. Josten, U. Koch, C. Hoessbacher, F. Ducry, L. Juchli, A. Emboras, D. Hillerkuss, M. Kohl, L. R. Dalton, C. Hafner, and J. Leuthold, Nat. Photonics **9**, 525 (2015).
[33]L. Alloatti, R. Palmer, S. Diebold, K. P. Pahl, B. Chen, R. Dinu, M. Fournier, J.-M. Fedeli, T. Zwick, W. Freude, C. Koos, and J. Leuthold, Light: Sci. Appl. **3**, e173 (2014).
[34]X. Zhang, C.-J. Chung, A. Hosseini, H. Subbaraman, J. Luo, A. K.-Y. Jen, R. L. Nelson, C. Y.-C. Lee, and R. T. Chen, J. Lightwave Technol. **34**, 2941 (2015).
[35]C. Doerr, J. Heanue, L. Chen, R. Aroca, S. Azemati, G. Ali, G. McBrien, L. Chen, B. Guan, and H. Zhang, in *Optical Fiber Communications Conference and Exhibition (OFC)* (IEEE, 2017), pp. 1–3.
[36]H. Subbaraman, X. Xu, A. Hosseini, X. Zhang, Y. Zhang, D. Kwong, and R. T. Chen, Opt. Express **23**, 2487 (2015).
[37]J. F. Coward, C. H. Chalfant, and P. H. Chang, J. Lightwave Technol. **11**, 2201 (1993).